**Tailoring the crystal structure of CaTiO3 by multielement doping for photo-assisted activation of NO**

**Reference:**
Y. Ji; B. Ding; W. Ni, et al., Tailoring the crystal structure of CaTiO3 by multielement doping for photo-assisted activation of NO. Chem. Eng. J. 2022, 450, 138255.

ISSN 1385-8947 (2022), Copyright © 2022 Elsevier B.V. All rights reserved
Full text (Publisher's DOI): https://doi.org/10.1016/j.cej.2022.138255
Received 20 April 2022, Revised 8 July 2022, Accepted 20 July 2022, Available online 25 July 2022, Version of Record 4 August 2022

# Tailoring the crystal structure of $CaTiO_3$ by multielement doping for photo-assisted activation of NO

Yilong Ji [a, ‡], Bo Ding [a, ‡], Wen Ni [b], Xiazhang Li [c], Xiaojun He [a, d], Zhiyuan Chen [e], Songlin Ran [b], Huihong Lü [a, d, *]

[a] Key Laboratory of Metallurgical Emission Reduction and Resources Recycling (Ministry of Education) & School of Chemistry and Chemical Engineering, Anhui University of Technology, Maanshan, China

[b] Anhui Provincial Key Lab of Metallurgical Engineering & Resources Recycling, Anhui University of Technology, Maanshan, China

[c] Jiangsu Key Laboratory of Advanced Catalytic Materials and Technology, Advanced Catalysis and Green Manufacturing Collaborative Innovation Center, Changzhou University, Changzhou 213164, PR China

[d] Anhui International Research Center of Energy Materials Green Manufacturing and Biotechnology, Anhui University of Technology, Maanshan, China

[e] Separation and Conversion Technology, Flemish Institute for Technological Research, 2400, Mol, Belgium

[‡] Both authors contributed equally to this work.

**Corresponding author:** Huihong Lü

**Corresponding email:** lv_huihong@163.com

**Address:** Hudong Road 59 Ma'anshan, Anhui, PR China

**Code:** 243002

**Fax & Tel:** 86-555-2311879

**Abstract:** Although photocatalysis exhibits great prospects in selective catalytic reduction of $NO_x$ (photo-SCR), the principles for the informed design of photo-SCR catalysts are lacking. Herein, based on inert $CaTiO_3$, we tailor a crystal structure for high-efficiency de$NO_x$ by partially substituting Ca with Ce, and Ti with Fe and Mn. The pristine $CaTiO_3$ is hard to remove NO in 100-300°C, while Ce-Fe-Mn doped $CaTiO_3$ could achieve nearly 100% NO conversion at 135°C under light irradiation (GHSV = 72000 $h^{-1}$). The dopants enable $CaTiO_3$ to activate NO and harvest visible light. By selectively activating gaseous molecules, Ti, Fe, and Mn present significant synergistic effects on accelerating the catalytic cycle of standard SCR. Moreover, it is firmly shown that the photocarriers intensify NO oxidation rather than $NH_3$-to-$NH_2$ transformation. This work provides new insights into the structure-activity relationship of perovskite-based catalysts and deepens the understanding of the light-driven mechanism.

**Keywords:** photocatalysis; perovskite; selective catalytic reduction; element doping; NO activation

## 1. Introduction

Cost-effective construction of $NH_3$-SCR catalytic systems to realize $NO_x$ removal in the low-temperature range has become urgent given the increasingly stringent environmental requirements. Since Tanaka group [1, 2] sparked the interest in photo-assisted selective catalytic reduction of NO (photo-SCR), a wealth of seminal studies [3-6] have proved that photoirradiation is pretty efficacious in ameliorating NO conversion and $N_2$ selectivity in the low-temperature range. Although great achievements have been made in this field, to date, we still lack enough recognition of principles for constructing photo-SCR catalysts.

There are three fundamental issues that plague us. The first is that the reaction mechanism of $NH_3$-SCR is disputed. $NH_2NO$ and $NH_4NO_2$ are the two principal intermediates of standard SCR, which form following the Eley-Rideal (E-R) and Langmuir-Hinshelwood (L-H) mechanisms, respectively. The main point of contention is whether the catalytic cycle entails the involvement of $NH_4NO_2$. [7-11] Some researchers [10, 12] proposed that whether $NH_4NO_2$ prevails depends on the catalyst nature and reaction temperature. Inexplicably, even for catalysts of the same ingredients, different reaction pathways have been reported. [10, 13] The inherent complexity of the $NH_3$-SCR reaction mechanism makes the informed construction of catalyst difficult.

The second issue is that the functions of photocarriers on catalytic redox are unclear. [14] The mainstream view [15-18] believed that light irradiation facilitates the transformation of chemisorbed $NH_3$ to $NH_2$ radical, thus accelerating the formation of the unstable intermediate $NH_2NO$ proceeding via Eley-Ride kinetics. Recently, by illuminated *in situ* DRIFTS, Gang et al. [19] found that photoirradiation could

drive the oxidation of NO into nitrite and nitrate over Fe-doped $TiO_2$. However, two questions remain to be answered : (i) is this promotional effect applicable to other types of photocatalysts, such as perovskites? (ii) could the photocarriers transform the chemisorbed $NH_3$ to $NH_2$ species? Therefore, this fundamental issue about the light-driven effect has not been systematically conclusive.

The last is the elusive correlation between surface activity and optical property, both of which are intrinsically determined by the electronic structure of the catalyst. For perovskite oxides of the $ABO_3$ formula, the electron occupancy in $e_g$ orbitals of the B-site element has been demonstrated as a useful descriptor to approximate the strength of adsorbate binding to the surface.[20] Modifying the crystal structure also impacts the optical property, along with the quantum efficiency. [21, 22] The major challenge of photocatalyst design lies in how to tailor the crystal structure to harmonize the molecule adsorption and light response.

The perovskite structure is flexibly tunable since both A and B sites are easily doped by other elements. [23, 24] Previously, our group [16, 25] reported that perovskite-based catalysts have excellent photoactivity for NO removal, and doping perovskite with transition metal ions could evidently improve its performance. In this work, we choose the inert $CaTiO_3$ as a basal material and construct an efficient structure for photo-SCR de$NO_x$ by doping it with Ce, Fe, and Mn elements. From Mn doping to Ce-Fe-Mn doping, each step modifies the crystal structure of $CaTiO_3$, making it increasingly elaborate and efficient. By combining experiments with DFT calculations, a systematic investigation into the relationships between intrinsic activity and crystal structure is implemented, as well as the light-driven mechanism.

## 2. Experiments

### *2.1. Materials*

The perovskite-based catalyst was directly extracted from Ti-bearing blast furnace slag (Ti-slag), which is a kind of metallurgical solid waste. More details about Ti-slag could be acquired in the supporting material. The Ti-slag was provided by Pangang Group Co., Ltd., China, and its chemical analysis is shown in Table S1. The slag was crushed, ground and sieved through a 200-mesh sieve before use. Unless otherwise specified, all of the rest reagents used in this study were of analytical grade and provided by Sinopharm Chemical Reagent Co., Ltd., China.

### *2.2. Catalyst preparation*

To obtain the target perovskite from Ti-slag, a process involving mineral phase reconstruction followed by acid leaching was adopted. To be specific, a powder mixture composed of 100.0 g of Ti-slag, 23.0 g of NaOH, 10.0 g of $MnO_2$, 5.0 g of $Fe_2O_3$, and 5.0 g of $CeO_2$ was placed in the MgO crucible and roasted at 1400°C for one hour. As the sintered sample was cooled to room temperature, it was crushed and ground into fine particles for acid leaching and characterization.

15.0 g of the sintered sample power was placed in a glass beaker of 500 mL, and then 225 mL of 8 % hydrochloric acid was added into the beaker. The mixture was stirred with a Teflon agitator at 25°C for 60 min. In this way, almost all the aluminosilicates were dissolved and transferred into the solution. After the slurry was filtered, the solid residue was dried at 105 °C for four hours for further analysis. The as-

obtained sample was denoted as 5Ce5Fe10Mn, in which the number represents the mass ratio of the following oxide to Ti-slag. Likewise, the label '10Mn' meant that the mass ratio of $MnO_2$ to Ti-slag in the powder mixture was 10%, and neither $CeO_2$ nor $Fe_2O_3$ was incorporated into the mixture.

*2.3. Catalyst characterization*

X-ray diffraction (XRD) patterns were collected by the Rigaku X-ray diffractometer (Ultima IV) with Cu K〈 radiation. Mineralogy analysis of the specimen was performed by field emission scanning electron microscopy (SEM, JSM-6490LV) equipped with an Oxford energy dispersive X-ray spectroscope (EDS). Morphology analysis was carried out by scanning transmission electron microscopy in high-angle annular dark field (HAADF-STEM, FEI TalosF200x). The high-resolution mapping of elements was implemented by Super-X EDS.

Fe and Mn K-edge EXAFS measurements were carried out at the BL01B1 beamline at Spring-8 of the Japan Synchrotron Radiation Research Institute (JASRI). Ce $L_{III}$-edge EXAFS measurement was collected at the Beamline of TPS44A1 in National Synchrotron Radiation Research Center (NSRRC). All the measurements were performed at room temperature, and XAFS data were recorded in fluorescent mode. The X-ray energy was calibrated using Fe and Mn foils, and the data analyses were performed utilizing Athena and Artemis in the Demeter software package.

0.10 g of Ti-slag was put into a 250mL Teflon beaker. Subsequently, 0.25 mL of hydrofluoric acid, 1.5 mL of hydrochloric acid, and 0.5mL of nitric acid were added to the beaker. The solution was kept heating until uniform bubbles were produced. Then, add 0.5 mL of 9M sulfuric acid into the solution and heat the solution again. When white smoke generates, the heating was kept for another 5 minutes. Next, boil the solution again after 1.5 mL of deionized water was added. When the solution was cooled to room temperature, it was diluted and analyzed by inductively coupled plasma–mass spectrometry (ICP-MS).

X-ray photoelectron spectra (XPS) were recorded on a Thermo Scientific K-Alpha spectrometry using Al K〈 irradiation. Raman spectra were obtained by the Renishaw Raman spectrophotometer. UV-vis diffuse reflectance spectra (DRS) of the specimens were recorded by a PerkinElmer Spectrometer (Lambda 950). The specific surface area of the specimen was measured by Brunauer-Emmett-Teller (BET) method. Both temperature-programmed reduction of $H_2$ ($H_2$-TPR) and desorption of $NH_3$ ($NH_3$-TPD) were implemented on a Huasi instrument (DAS-7000).

*In situ* DRIFT experiments were performed on a Nicolet 6700 spectrometer in the wavenumber range of 2000 to 1000 $cm^{-1}$ with 4 $cm^{-1}$ resolution. *In situ* IR spectra were collected on a PerkinElmer spectrometer in the wavenumber range of 2000 to 800 $cm^{-1}$ with 4 $cm^{-1}$ resolution. The detailed procedures for *in situ* IR spectrum are as follows. First, the specimen was treated at 300 °C under $N_2$ flow for 0.5 h to remove the species adsorbed on the specimen surface. Second, the specimen was regulated to the target temperature to obtain a background spectrum which should be subtracted from the specimen spectrum. Then, the specimen was exposed to a flow of 1000 ppm $NH_3$ or 1000 ppm NO + 3 vol% $O_2$ for one hour, and the IR spectrum in the dark was recorded. Finally, the Xe lamp was turned on, and the IR spectrum under light irradiation was collected 15 min later.

*2.4. Catalytic activity test*

The SCR activity was tested in a fixed-bed reactor equipped with a Xenon lamp. The simulated gas consisted of 1000 ppm NO, 1000 ppm $NH_3$, 3 vol% $O_2$, and a balance of $N_2$, corresponding to a gas hourly space velocity (GHSV) of 72000 $h^{-1}$. Both NO and $NO_2$ were determined by a BUV150 flue gas analyzer, $NH_3$ determined by a BLD200 analyzer, and $N_2O$ by a BGM250 analyzer. During the catalytic process, the reactor was cooled by circulating water to offset the temperature fluctuation caused by light irradiation. The NO conversion percentage and $N_2$ selectivity were calculated by the following formula:

$$\text{NO conversion (\%)} = \frac{[NO]_{in}-[NO]_{out}}{[NO]_{in}} \times 100\% \quad (1)$$

$$N_2 \text{ selectivity} = \left(1-\frac{2[N_2O]_{out}}{[NO]_{in}+[NH_3]_{in}-[NO]_{out}-[NH_3]_{out}}\right)\times 100\% \quad (2)$$

*2.5. Computational details*

The structural relaxation and singlet energy point energy calculations were performed using the density functional theory (DFT) method as implemented in Vienna Ab initio Simulation Package (VASP) [26, 27]. The generalized gradient approximation (GGA) in the form of Perdew-Burke-Ernzerhof (PBE) functional was used to evaluate the exchange-correlation potential[28]. The project-augmented wave approach was employed to represent the core-electron interaction. The atomic orbitals treated as valence states were as follows: 3*s*3*p*4*s* of Ca, 3*d*4*s* of Ti, 3*p*3*d*4*s* of Mn, 3*p*3*d*4*s* of Fe, and 2*s*2*p* of O. Hubbard corrections with $U_{eff}$ = 5.3 eV and 3.9 eV were applied to describe the 3d-orbitals of Fe and Mn atoms, respectively.

The lattice constant of relaxed bulk $CaTiO_3$ was 5.36×5.46×7.62 Å, in reasonable agreement with the experimental value of 5.38×5.44×7.64 Å (PDF 078-1013) [29]. A periodic $CaTiO_3$ (001) slab separated by a vacuum layer of 15 Å was built from this lattice. In total, there are 80 atoms in each slab, containing 16 Ca, 14 Ti, 1 Mn, 1 Fe, and 48 O. The self-consistent field method with the tolerance of $1.0\times10^{-6}$ eV/atom and the plane wave basis sets with an energy cutoff of 500 eV were adopted. The structural optimization was relaxed until the Hellman-Feynman force on each ion was less than 0.02 eV/Å.

Adsorption energies of gas molecules, $E_{ads}$, in this paper were calculated as the following equation:

$$E_{ads} = E_{slab+gas} - E_{slab} - E_{gas} \quad (3)$$

where $E_{slag+gas}$ is the total energy of the perovskite slab with a gas molecule bound to it, $E_{slab}$ is the total energy of the clean $CaTiO_3$ slab, and $E_{gas}$ is the total energy of the gas molecules.

## 3. Results

*3.1. Synthesis and catalyst characterization*

*3.1.1 Catalyst synthesis*

All the perovskite samples are extracted from Ti-bearing blast furnace slag (Ti-slag) using a molten salt method followed by acid leaching. By roasting Ti-slag with NaOH at 1400°C, a molten system consisting of $Na_2O$-CaO-MgO-$TiO_2$-$Al_2O_3$-$SiO_2$ was acquired. With the decrease in temperature, $CaTiO_3$ crystallized from the molten salt, and the rest formed a zeolite phase (Fig. S1). Three metal

oxides, including $CeO_2$, $Fe_2O_3$, and $MnO_2$, are also added to the mixture to modify $CaTiO_3$. EDS mapping analysis on the roasted slag in Fig. 1a illustrates that most of Ca, Ti, Ce, and Mn are preferentially concentrated in the perovskite, while Na, Mg, Al, and Si are enriched in the zeolite. The distribution of Fe shows little difference between perovskite and zeolite, perhaps due to its considerable solubility in both two phases. The zeolite is easily removed by acid leaching, and thus high-purity perovskite samples are obtained.

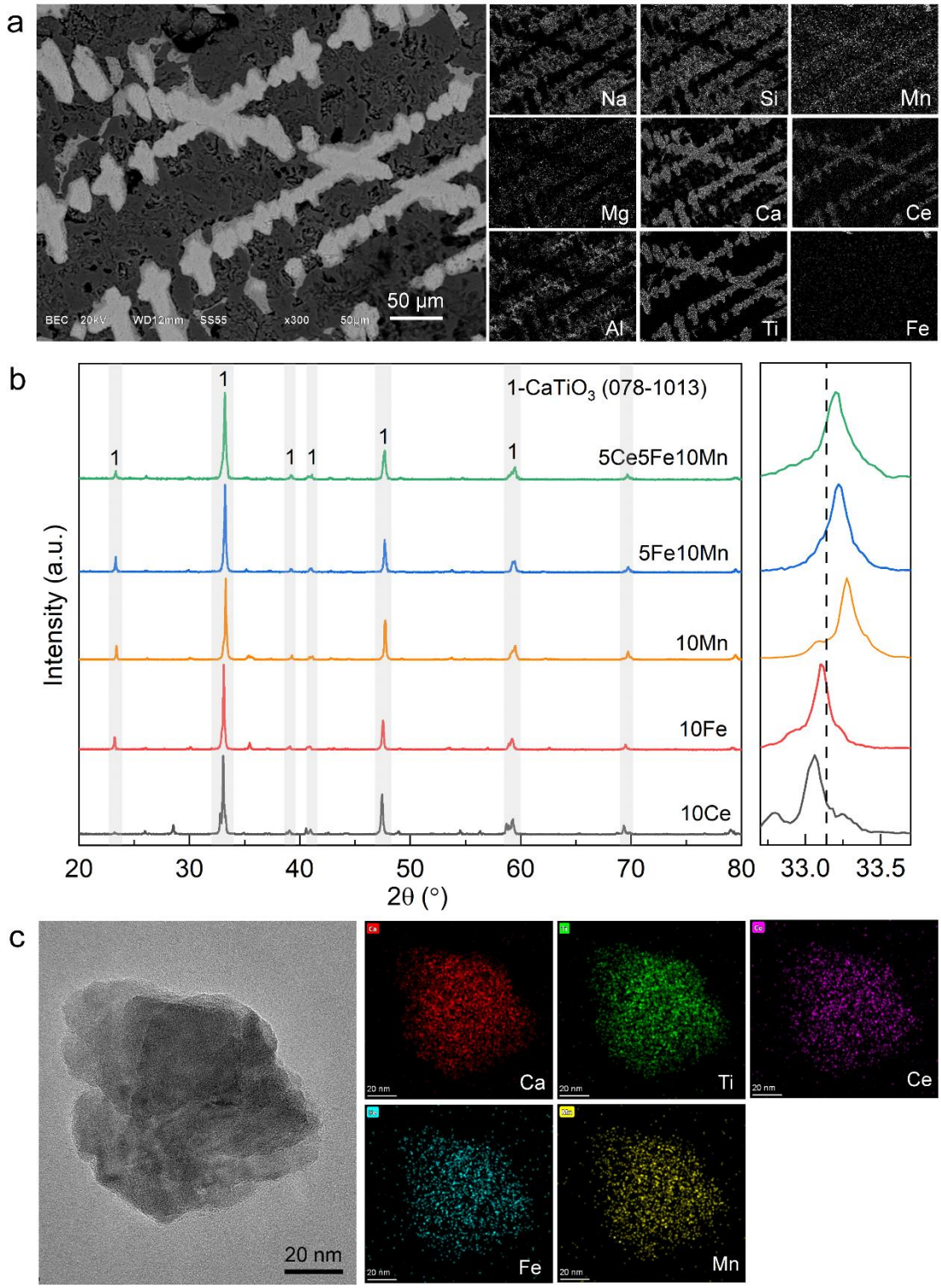


**Fig. 1. Phases and morphology of the roasted oxides and perovskite sample. a**, Typical section morphology and

element mapping of the composite oxides (1400°C-roasted Ti-slag with NaOH, $CeO_2$, $Fe_2O_3$, and $MnO_2$) obtained by SEM and EDS analysis. **b**, XRD patterns of the perovskite samples. The right part is the high-resolution XRD patterns within 32.7° to 33.7°. The dashed line denotes the position of the (112) peak from pure $CaTiO_3$. **c**, HAADF-STEM image and EDS mapping of sample 5Ce5Fe10Mn.

The perovskite obtained by introducing 10 wt% $CeO_2$ is designated as 10Ce, and so on. The chemical compositions of the resultant samples are listed in Table S2 and S3, respectively. All the adscititious metal oxides are well incorporated into the samples, such as 19.7 wt% $CeO_2$ of 10Ce, 12.0 wt% $Fe_2O_3$ of 10Fe, and 10.4 wt% MnO of 10Mn. XRD analysis in Fig. S1b demonstrates that each sample is comprised of a perovskite phase. The (112) peaks from both 10Ce and 10Fe shift to the left relative to pure $CaTiO_3$, showing that either Ce or Fe doping enlarges the unit cell. Conversely, Mn doping (10Mn) causes a right shift of (112) peak, lessening the lattice.

*3.1.2 Morphology and crystal structure*

The morphology of the 5Ce5Fe10Mn specimen is investigated by HAADF-STEM and displayed in Fig. S3. In general, the particles from 5Ce5Fe10Mn are irregular and vary from dozens to several hundred nanometers. Elemental mapping on a typical particle (Fig. 1c) revealed that Ca, Ti, Fe, Ce, and Mn uniformly disperse in the particle at the nanometer scale. Hence, the dopants of Ce, Fe, and Mn are incorporated into the $CaTiO_3$, forming a homogeneous solid solution rather than a mixture of metal oxides.

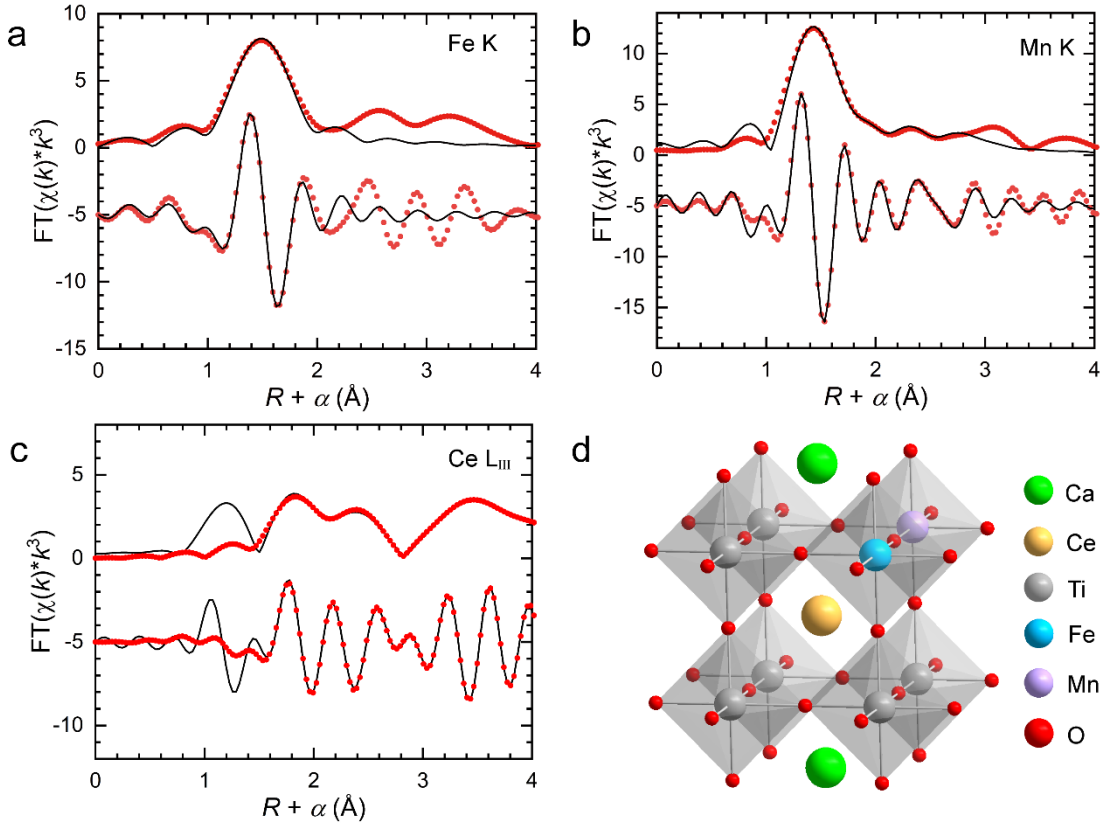


**Fig. 2. Crystal structure of the perovskite sample. a**, Fe K-edge EXAFS (points) and curvefit (line) for 5Ce5Fe10Mn, shown in *R*-space (FT magnitude and imaginary component); **b**, Mn K-edge EXAFS (points) and curvefit (line) for 5Ce5Fe10Mn; **c**, Ce $L_{III}$-edge EXAFS (points) and curvefit (line) for 10Ce. All the data are $k^3$-weighted and not phase-corrected; **d**, Diagram of the crystal structure of $CaTiO_3$ doped with Ce, Fe, and Mn.

EXAFS spectra of 5Ce5Fe10Mn and 10Ce samples are recorded to reveal the positions of dopants in perovskite (Fig. 2). The Fourier-transformed k-space EXAFS spectra are displayed in Fig. S4, and the

fitting parameters are placed in Table S4-S6. The fitted coordination number of the Fe atom in 5Ce5Fe10Mn is 6.0. The coordination number of Mn atom is constrained as 6.0 in the fitting for Mn K-edge EXAFS spectra, and the R factor is returned as 1.5%. These results confirmed that both Fe and Mn substitute Ti in $CaTiO_3$ and occupy the B sites. Constraining the coordination number of Ce atom as 12.0 returns 0.5% of the R factor, substantiating that Ce substitutes Ca and occupies the A site. A diagram is presented in Fig. 2d to illustrate the crystal structure of Ce-Fe-Mn doped $CaTiO_3$.

*3.1.3 Surface properties*

The specific surface areas of the samples are in a range of 14.9-16.5 $m^2/g$ (Table S7), and the pore volumes are in 0.022-0.033 $cm^3/g$. The two parameters are almost one magnitude less than the nanocomposites fabricated by homogeneous precipitation[30], probably because the samples are prepared by a high-temperature process.

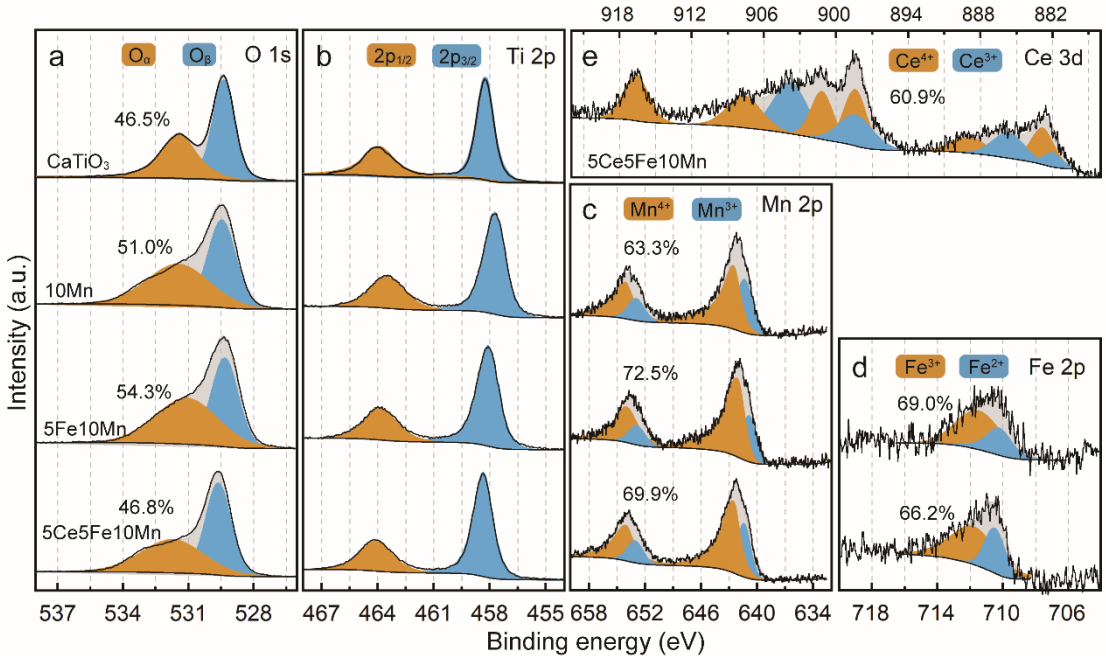


**Fig. 3 XPS of $CaTiO_3$ and doped $CaTiO_3$.** a, O 1s; b, Ti 2p; c, Mn 2p; d, Fe 2p; e, Ce 3d.

XPS analysis was implemented to probe the valence states of the surface ions from pure $CaTiO_3$ and doped $CaTiO_3$. The O 1s curve (Fig. 3a) could be deconvoluted into two peaks located at 531.0-531.7 eV and 529.2-529.7 eV, which are assigned to chemisorbed labile oxygen species ($O_\alpha$) and lattice oxygen in the perovskite ($O_\beta$), respectively. The $O_\alpha$ ratio of pure $CaTiO_3$, $O_\alpha/(O_\alpha + O_\beta)$, is calculated as 46.5%. With the incorporation of 10% $MnO_2$, the peak shape of $O_\alpha$ becomes wider, suggesting that the chemisorbed oxygen species on 10Mn have more types of geometric configurations, such as $O_2$ adsorbed on the Ti site and $O_2$ adsorbed on the Mn site. The $O_\alpha$ ratio of 10Mn is increased to 51.0%. Further introducing 5% $Fe_2O_3$ into 10Mn increases the $O_\alpha$ ratio to 54.3%, while incorporating 5% $CeO_2$ into 5Fe10Mn dramatically decreases the $O_\alpha$ ratio to 46.8%. The differences in the chemisorbed oxygen species between perovskites intrinsically result from various metal sites introduced by the dopants.

The Ti 2p curves in Fig. 3b consist of a pair of spin-orbit doublets, which could be indexed to Ti $2p_{1/2}$ (463.5-464.1 eV) and Ti $2p_{3/2}$ (457.7-458.3 eV), respectively. The valence states of surface Ti ions from perovskites are sensitive to the dopants. Specifically, the Ti $2p_{3/2}$ peak from pure $CaTiO_3$ is centered at

458.2 eV. This peak from 10Mn has a right shift and is around 457.7 eV, signifying that some valency electrons transfer from the Mn ions to the Ti ions. The Ti $2p_{3/2}$ peaks from 5Fe10Mn and 5Ce5Fe10Mn are at 458.1 eV and 458.3 eV, respectively. These two values are close to that of pure $CaTiO_3$ (458.2 eV), indicating that the changes in the valence states of surface Ti ions are subtle if $CaTiO_3$ is simultaneously doped with Fe-Mn or Ce-Fe-Mn.

The Mn 2p curves in Fig. 3c could be fitted by four peaks, which are assigned to $Mn^{3+}$ and $Mn^{4+}$, respectively. The $Mn^{4+}$ ratio of 10Mn, $Mn^{4+}/(Mn^{3+} + Mn^{4+})$, is 63.3%. With the incorporation of 5% $Fe_2O_3$ into 10Mn, the $Mn^{4+}$ ratio apparently rises to 72.5%. As p-type doping, the substitution of $Ti^{4+}$ by the low-valence $Fe^{3+}$ leads to the decrease in valency electrons transferring to O ions. In this case, the Mn ions have to provide more electrons, explaining why the $Mn^{4+}$ ratio of 5Fe10Mn is increased in comparison with that of 10Mn. Likewise, as n-type doping, the substitution of $Ca^{2+}$ by the high-valence $Ce^{3+}$ or $Ce^{4+}$ introduces excess electrons, decreasing the $Mn^{4+}$ ratio of 5Ce5Fe10Mn to 69.9%.

The Fe 2p curves in Fig. 3d are deconvoluted into two peaks at 711.5-711.8 eV and 710.2-710.5 eV, ascribed to $Fe^{3+}$ and $Fe^{2+}$, respectively. The $Fe^{3+}$ ratio of 5Fe10Mn, $Fe^{3+}/(Fe^{3+} + Fe^{2+})$, is 69.0%, while that of 5Ce5Fe10Mn slightly decreases to 66.2%. The effect of Ce doping could also interpret the variation of the $Fe^{3+}$ ratio. Besides, the Ce 3d curve in Fig. 3e is fitted by ten peaks, comprising six orange peaks assigned to $Ce^{4+}$ and four blue peaks to $Ce^{3+}$. The $Ce^{4+}$ ratio of 5Ce5Fe10Mn, $Ce^{4+}/(Ce^{4+} + Ce^{3+})$, is calculated as 60.9%.

On the whole, two conclusions could be summarized from the XPS results. First, there is a noticeable charge transfer between diverse metal ions when the perovskite is doped with other metal elements. This phenomenon occurs not only between the B-site metal ions but also between the A-site and B-site metal ions, implying that the A site also plays a role in the activity of the B site. Second, the chemical valence of surface metal ions from perovskites could be increased by the p-type doping and decreased by the n-type doping.

*3.2. $NH_3$-SCR activity of single-element doped $CaTiO_3$*

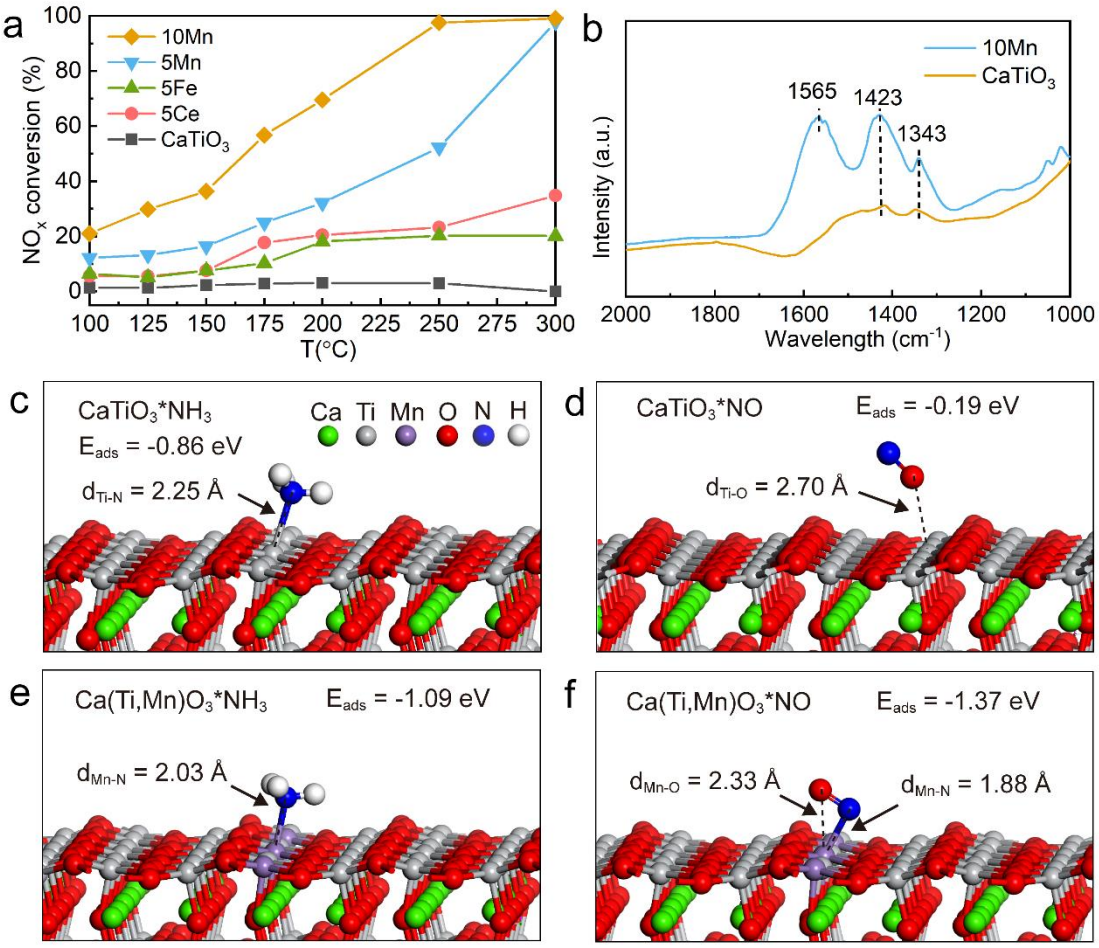


**Fig. 4. $NH_3$-SCR activity of single-element doped $CaTiO_3$. a**, Temperature-dependent $NO_x$ conversion over $CaTiO_3$ doped with a single element in the dark.( 1000 ppm NO, 1000 ppm $NH_3$, 3 vol% $O_2$, GHSV = 72000 $h^{-1}$). **b**, *In situ* DRIFT of $CaTiO_3$ and 10Mn with NO + $O_2$ adsorbed at 25°C in the dark. The adsorption of $NH_3$ (**c**) and NO (**d**) on the $TiO_2$-(001) termination of $CaTiO_3$; the adsorption of $NH_3$ (**e**) and NO (**f**) on the $TiO_2$-(001) termination of Ca(Ti, Mn)$O_3$.

The pure $CaTiO_3$ is hard to remove $NO_x$ in 100-300°C (Fig. 4a). After introducing Ce, Fe, or Mn, the modified $CaTiO_3$ becomes active, showing that both A and B sites are responsible for the catalytic activity of perovskite. In terms of identical doping amount in mass ratio, 5Mn is superior to 5Ce and 5Fe. In particular, 10Mn could achieve 97.7% $NO_x$ conversion at 250°C, exhibiting the apparent advantage of Mn doping to gift $CaTiO_3$ denitration activity.

*In situ* DRIFTS spectra of adsorbing NO + $O_2$ over $CaTiO_3$ and 10Mn were given in Fig. 4b. Three strong bands peaking at 1565 $cm^{-1}$, 1423 $cm^{-1}$, and 1343 $cm^{-1}$ from 10Mn are assigned to bidentate nitrate, nitro compounds, and bridged nitrites, respectively. However, all the three bands from $CaTiO_3$ are quite weak, indicating that pure $CaTiO_3$ is difficult to activate gaseous NO molecule.

DFT calculations were performed to further investigate the effect of Mn doping on $CaTiO_3$ activity. The (001)-plane termination exposing $TiO_2$ units is chosen as a basal surface of $CaTiO_3$, which is relatively stable under the anoxic condition. [31, 32] As shown in Fig. 4c, pure $CaTiO_3$ is capable of adsorbing $NH_3$ on the five-coordinated ($Ti_{5c}$) site with an adsorption energy of -0.86 eV, but hard to capture NO as the adsorption energy is -0.19 eV (Fig. 4d). With the introduction of Mn into $CaTiO_3$ (Fig.

S5), the adsorption energy of $NH_3$ slightly increases to -1.09 eV (Fig. 4e). Intriguingly, NO could bond strongly to the $Mn_{5c}$ site of Ca(Ti, Mn)$O_3$ ($E_{ads}$ = -1.37 eV) as a bidentate anion carrying 0.20 electrons according to Bader charge analysis (Fig. 4f).

The adsorption configuration of NO on $MnO_5$ pyramids well satisfies the requirement of spatially symmetric overlap between NO $\pi^*$ orbitals and $MnO_5$ $e_g$ orbitals. [33] The redundant electrons in NO anion prefer occupying the antibonding orbital $2\pi$ of NO, weakening the N-O bond so that the chemisorbed NO is vulnerable to the lattice or chemisorbed oxygens to generate $NO_2$ (fast SCR) [34-38], or the chemisorbed $NH_3$ on adjacent $Ti_{5c}$ to yield intermediate $NH_2NO$ (L-H pathway). As depicted in Fig. S6, the formation of $NH_2NO$ on the surface of Mn-doped $CaTiO_3$ is energetically favorable. Therefore, the SCR activity of Ca(Ti, Mn)$O_3$ derives from the activation of NO by the $Mn_{5c}$ site.

### *3.3. $NH_3$-SCR activity of multielement doped $CaTiO_3$*

Compared with 10Mn, the activity of 5Fe10Mn is significantly improved in 100-300°C (Fig. 5a). The $NO_x$ conversion over 5Fe10Mn reached 99% at 175°C, far more than the sum of these over sole 5Fe and 10Mn (Fig. 4a). Fe-Mn doping of $CaTiO_3$ presents synergistic effects on removing $NO_x$. Nevertheless, if we continued doping 5Fe10Mn with 5 wt% $CeO_2$, the performance showed little difference between 5Ce5Fe10Mn and 5Fe10Mn in 100-300°C (Fig. 5a).

The redox behaviors of 10Mn and 5Fe10Mn were investigated by $H_2$-TPR experiments (Fig. 5b). The strongest peak from 10Mn is centered at 604.4°C, and that from 5Fe10Mn at 566.3°C. Fe addition shifts the reduction peak to the lower temperature, enhancing the diffusion of $O^{2-}$ anion within the lattice. [39] This might be partially ascribed to the oxygen vacancies introduced by the p-type doping of perovskite, which facilitates the movements of electrons and oxygen ions. [40] The oxygen vacancies also provide energetically favorable connection channels for gaseous $O_2$ molecules, triggering the dissociation of $O_2$ into O atoms, further expediting NO oxidation. [41] However, given that the 5Fe sample is also a p-type doped perovskite, the synergetic effects between Fe and Mn could not be ascribed to the oxygen vacancies.

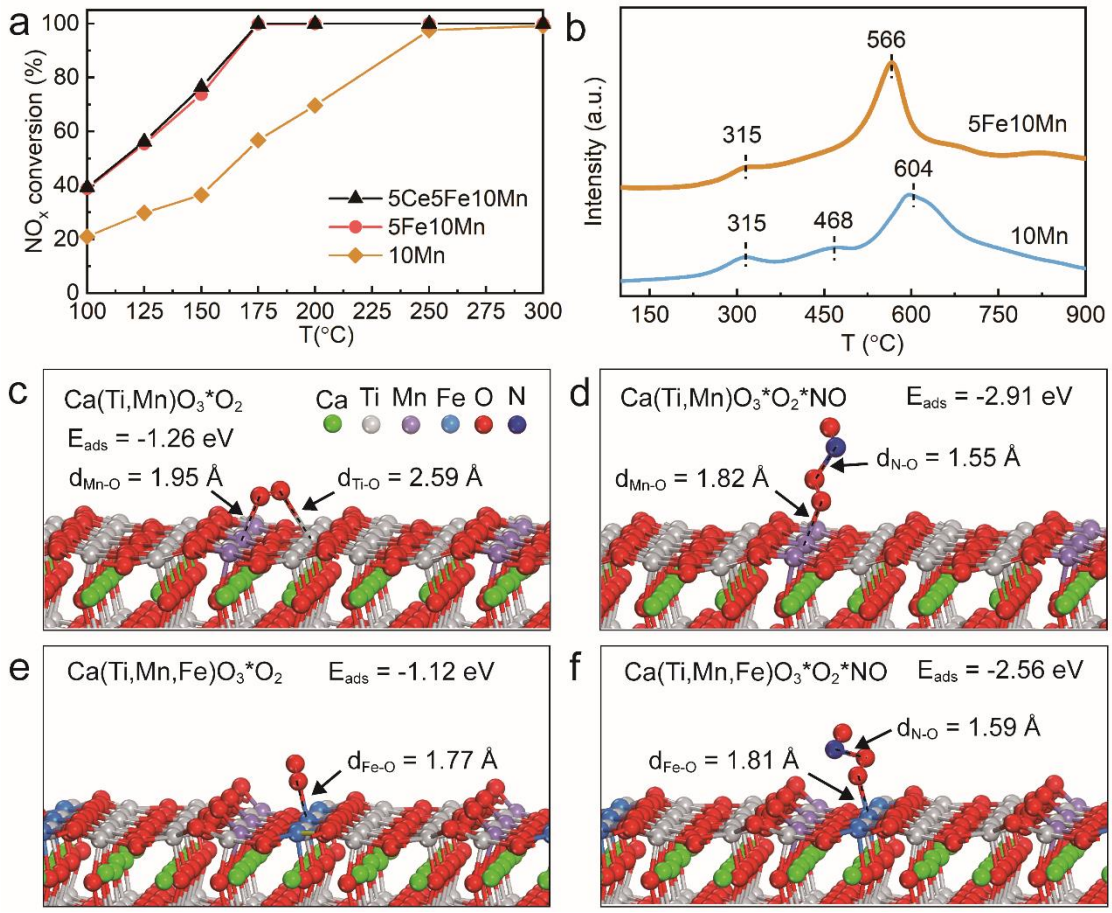


**Fig. 5. $NH_3$-SCR activity of multielement doped $CaTiO_3$. a**, Temperature-dependent $NO_x$ conversion over $CaTiO_3$ doped with multiple elements in the dark. (1000 ppm NO, 1000 ppm $NH_3$, 3 vol% $O_2$, GHSV = 72000 $h^{-1}$). **b**, $H_2$-TPR profiles of 10Mn and 5Fe10Mn. The adsorption of $O_2$ (**c**) and $O_2$ + NO (**d**) on the (Ti, Mn)$O_2$-(001) termination of Ca(Ti, Mn)$O_3$; the adsorption of $O_2$ (**e**) and $O_2$ + NO (**f**) on the (Ti, Mn, Fe)$O_2$-(001) termination of Ca(Ti, Mn, Fe)$O_3$.

To explore the underlying mechanism, the interactions between Ca(Ti, Fe, Mn)$O_3$ surface and gaseous molecules were examined by the DFT calculations. The mole ratio of Ti to Mn in 10Mn is about 3:1 (Table S2). A scheme about the ideal arrangement of B-site atoms in 10Mn is placed in Fig. S8a. Taking the lattice symmetry into account, three Ti sites could be substituted by the Fe ion. Specifically, two sites are adjacent to the Mn ion (Ti1 and Ti2), and a site is located at the diagonal position (Ti3). Clearly, the Fe ion has a higher probability of situating next to the Mn ion. The calculated energies (Fig. S8b and S8c) also show that the structure with Fe-Mn next to each other is more stable than the counterpart with Fe-Mn along the diagonal line. Therefore, the former model is adopted to investigate the Fe-Mn synergy. As shown in Fig. S7c, in this model, the $FeO_6$ and $MnO_6$ octahedra are conjoined with each other by a bridged oxygen.

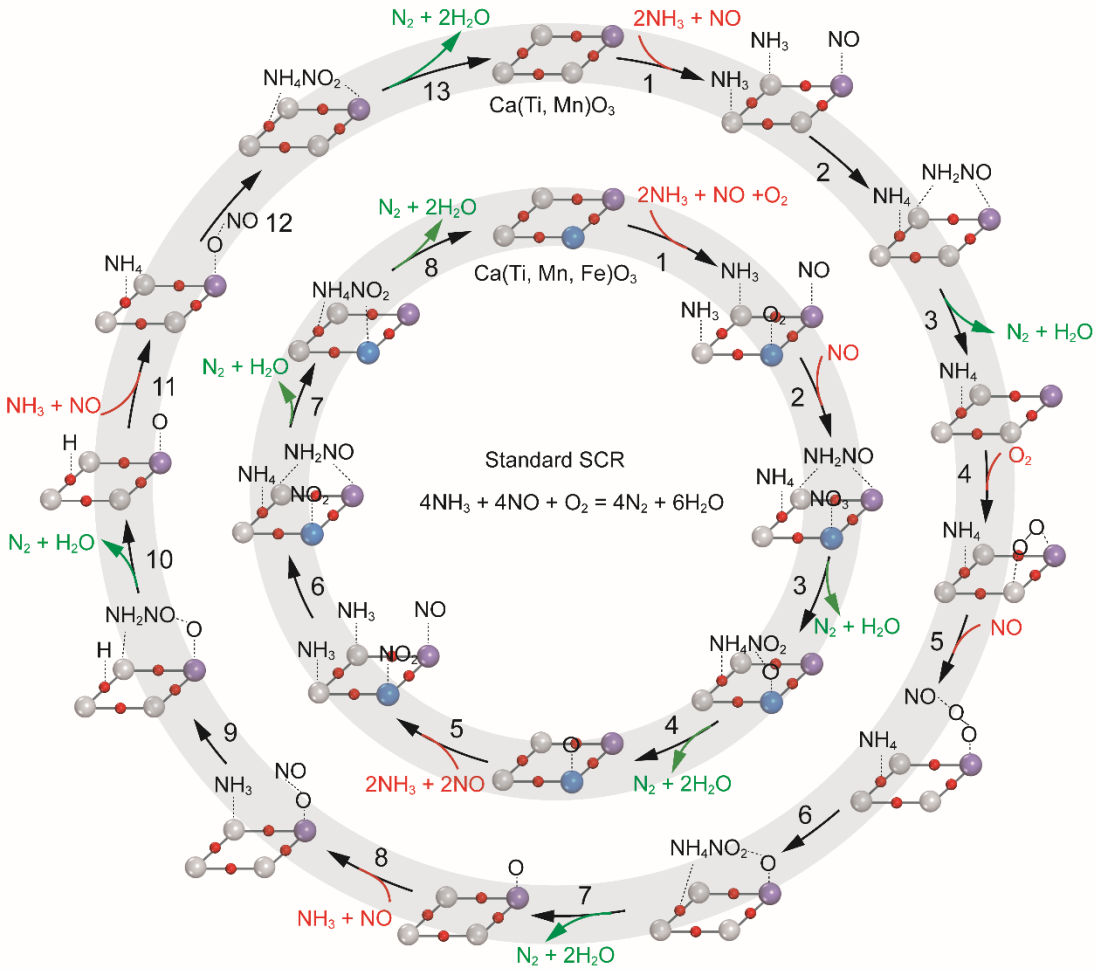


**Fig. 6. Proposed reaction pathways of Standard SCR over the perovskite.** The reaction pathways of the regeneration of active sites from Ca(Ti, Mn)$O_3$ (the outer ring) and Ca(Ti, Mn, Fe)$O_3$ (the inner ring) are partially based on the DFT calculations.

For Mn-doped $CaTiO_3$, the gaseous $O_2$ molecule prefers binding to the $Mn_{5c}$ and $Ti_{5c}$ sites with an adsorption energy of -1.26 eV (Fig. 5c). The chemisorbed $O_2$ could further combine with gaseous NO to produce monodentate nitrate binding to the $Mn_{5c}$ site ($\Delta E$ = -1.65 eV) as shown in Fig. 5d (Video S1). By contrast, for Fe-Mn doped $CaTiO_3$, the gaseous $O_2$ molecule selectively binds to the $Fe_{5c}$ site rather than the $Mn_{5c}$ or $Ti_{5c}$ site (Fig. 5e, $E_{ads}$ = -1.12 eV). The subsequently generated nitrate is still attached to the $Fe_{5c}$ site (Fig. 5f, $E_{ads}$ = -2.56 eV, Video S2). Transition state calculations in Fig. S9 disclose that the nitrate formations on the surface of both Ca(Ti, Mn)$O_3$ and Ca(Ti, Mn, Fe)$O_3$ have low reaction barriers (0.08 eV vs. 0.06 eV), revealing that this elementary reaction is not the determining step of the catalytic cycle. Adding Fe into Mn-doped $CaTiO_3$ converts the NO-to-$NO_3^-$ oxidative center from the $Mn_{5c}$ site to the $Fe_{5c}$ site. This conversion exerts a profound influence on the reaction pathway of the SCR process.

Based on DFT calculations, we propose two reaction routes to describe the standard SCR over Mn and Fe-Mn doped $CaTiO_3$. As shown in Fig. 6, the catalytic cycle over Ca(Ti, Mn)$O_3$ (the outer ring) comprises thirteen steps involving the $NH_2NO$ and $NH_4NO_2$ intermediates. [9, 11, 13] In this cycle, both intermediates bind to the $Mn_{5c}$ site. Thus, their formations have to proceed by sequence. With the addition of Fe, $O_2$ selectively binds to the $Fe_{5c}$ site. This increases the NO coverage on Mn5c sites and averts the cycle termination resulting from the case in Fig. S8d. Hence, step 2 of the inner ring is much more

favorable than the outer ring.

On the other hand, Fe ion provides a new site for the NO-to-$NO_3^-$ transformation so that $NH_4NO_2$ could form in tandem with the generation of $NH_2NO$. Consequently, the catalytic cycle over Ca(Ti, Mn, Fe)$O_3$ could be completed within eight steps (the inner ring in Fig. 6), markedly shortening the reaction pathway. Due to the selective adsorption of gaseous molecules, the active sites of Ti, Mn, and Fe display apparent synergistic effects on accelerating the catalytic cycle of standard SCR.

### *3.4. Photo-SCR activity of doped $CaTiO_3$*

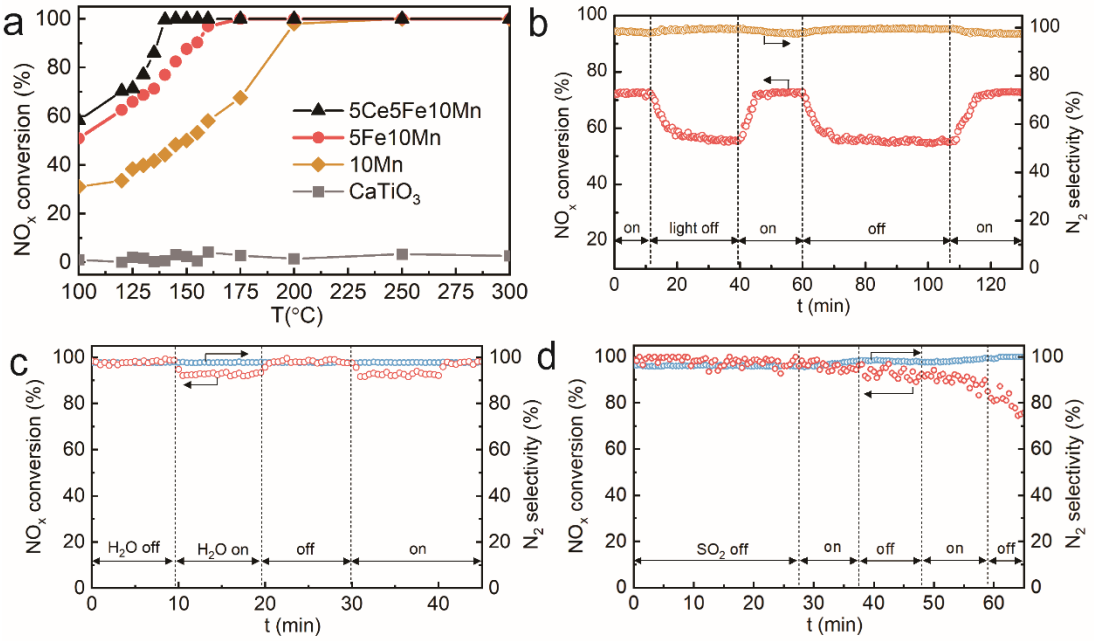


**Fig. 7. Photo-SCR activity of doped $CaTiO_3$. a,** Temperature-dependent $NO_x$ conversion over 10Mn, 5Fe10Mn, and 5Ce5Fe10Mn under visible light irradiation; **b**, Light on-off cycle tests over 5Ce5Fe10Mn at 125°C. Catalytic stability test of 5Ce5Fe10Mn at 150°C: c, 5 vol% $H_2O$; **d**, 100 ppm $SO_2$. (1000 ppm NO, 1000 ppm $NH_3$, 3 vol% $O_2$, GHSV = 72000 $h^{-1}$)

Under light irradiation, $CaTiO_3$ is still inert for NO removal (Fig. 7a), while the performance of doped $CaTiO_3$ is significantly improved, especially in 100-200°C. The 99%-conversion temperature over illuminated 5Ce5Fe10Mn is about 135°C, far lower than 175°C over ground-state 5Ce5Fe10Mn (Fig. 5a). As the light turns on at 125°C (Fig. 7b), $NO_x$ conversion over 5Ce5Fe10Mn rises from about 56% to 71% at 125°C without the decrease in $N_2$ selectivity, demonstrating that photocatalysis could serve as a green and effective technique to promote NO removal.

Table 1 lists the typical catalysts for $NH_3$-SCR de$NO_x$. Compared with the other catalysts, 5Ce5Fe10Mn shows excellent low-temperature activity, achieving almost 100% NO removal in the temperature range of 135-300°C with a relatively high GHSV of 72000 $h^{-1}$. Owing to the high-temperature preparation method, the specific surface area of 5Ce5Fe10Mn is much less than those of the porous nanoparticles. For instance, the BET specific surface area of Ce-Mn-Ti oxides in ref [42] is nearly ten times that of 5Ce5Fe10Mn (166.1 $m^2/g$ vs. 16.5 $m^2/g$). However, the performance of the latter regarding $NH_3$-SCR de$NO_x$ is superior to the former. We could ascribe the advantages of doped $CaTiO_3$ to two aspects. First, relative to the mixed oxides, the perovskite is more favorable for constructing precise structure by element doping, providing a possibility to regulate the reaction pathway of the

catalytic cycle toward efficient denitration. Second, light illumination, as a promising technique, also plays a notable role in SCR deNO$_x$.

**Table 1** Typical catalysts for NH$_3$-SCR deNO$_x$.

| Catalysts | Synthesis | Reaction conditions | NO conversion | ref |
|---|---|---|---|---|
| Ce-Mn-Ti oxides | Homogeneous precipitation | [NO] = [NH$_3$] = 500 ppm, GHSV = 30000 h$^{-1}$ | >90% (150-225°C) | [42] |
| Sn-doped TiO$_2$ | Coprecipitation | [NO] = [NH$_3$] = 500 ppm, GHSV = 79000 h$^{-1}$ | >90% (350-50°C) | [43] |
| Mn-Ni-Ti oxides | Homogeneous precipitation | [NO] = [NH$_3$] = 500 ppm, GHSV = 40000 h$^{-1}$ | >90% (340-460°C) | [44] |
| Ti-Mn-Fe oxides | Solution combustion method | [NO] = [NH$_3$] = 1000 ppm, GHSV = 40000 h$^{-1}$ | >90% (190-450°C) | [45] |
| Mn-Fe spinel | Coprecipitation | [NO] = [NH$_3$] = 500 ppm, GHSV = 150000 h$^{-1}$ | >80% (130-200°C) | [46] |
| W-V oxides | Oxalate method | [NO] = [NH$_3$] = 250 ppm, GHSV = 40000 h$^{-1}$ | ~100% (145-240°C) | [47] |
| 5Ce5Fe10Mn | Molten salt followed by acid leaching | [NO] = [NH$_3$] = 1000 ppm, GHSV = 720000 h$^{-1}$ | ~100% (135-300°C) | This work |

Catalytic stability tests were implemented to evaluate the performance of 5Ce5Fe10Mn at 150°C in the presence of H$_2$O and SO$_2$. With the input of 5 vol% water (Fig. 7c), the NO conversion was slightly decreased from about 98.7% to 92.8% without the decrease in N$_2$ selectivity. As the H$_2$O addition was turned off, the NO conversion rapidly increased to about 98.7% again. After the two-round cycle, the NO conversion could still keep above 98%, showing that 5Ce5Fe10Mn possesses outstanding water resistance and the suppression effect of water vapor on catalytic activities is reversible. In the presence of 100 ppm SO$_2$, the NO conversion slightly decreased from about 98.7% to 96.3%. Different from the variation with H$_2$O addition, the decrease in NO conversion by inputting SO$_2$ was gradual and irreversible when the SO$_2$ addition was turned off. After two rounds of SO$_2$ addition, the NO conversion dropped to about 84.5% and still declined with time. The negative effect of SO$_2$ was observable, probably due to the deposition of NH$_4$SO$_4$ at low temperatures.

### *3.5. The effect of light irradiation*

Pristine CaTiO$_3$ is hard to harvest the visible light due to its wide bandgap of 3.2 eV. By introducing dopants, the light wavelength absorbed by perovskite extends from the ultraviolet band to the visible band (Fig. 8a). The calculations on the projected density of states (Fig. 8b) disclose that Mn doping introduces an impurity band composed of Mn 3d and O 2p orbitals between the valance and conduction band. For Fe-Mn doped CaTiO$_3$, there are four impurity bands, including the donor levels composed of Fe 3d, Mn 3d, and O 2p orbitals below the Fermi level, and the acceptor levels composed of Mn 3d and O 2p orbitals above Fermi level. The impurity levels narrow the bandgap and enable the perovskite to harvest the visible light.

Although 5Ce5Fe10Mn shows little difference in NO removal with 5Fe10Mn in the dark (Fig. 5a), the former is notably superior to the latter under light irradiation (Fig. 7a). Li et al. [5] previously reported that PrFeO$_3$ doped with Ce displays a redshift of UV-vis absorption. Similar phenomena are observed in Fig. 8a. Relative to 5Fe10Mn, 5Ce5Fe10Mn exhibits enhanced light absorption in the wavelength range from 500 nm to 800 nm. The optimization of optical property by Ce doping improves the perovskite photoactivity.

To unravel photocarriers' roles in NO removal, *in situ* IR spectra of 5Ce5Fe10Mn with gaseous molecules adsorbed were recorded in the dark and light at 125°C. The dark spectra of $NH_3$-adsorbed 5Ce5Fe10Mn (black line in Fig. 8c) have four strong peaks. Two peaks around 931 $cm^{-1}$ and 966 $cm^{-1}$ are assigned to weakly absorbed $NH_3$ [48]; the one centered at 1250 $cm^{-1}$ corresponds to $NH_3$ coordinated on Lewis acid site, [47] and that around 1366 $cm^{-1}$ belongs to $NH_4^+$ bonded to Bronsted acid site. [49] The illuminated spectra (red line in Fig. 8c) vary little in comparison to the dark counterpart. Most peaks remain unchanged except for those at 1250 $cm^{-1}$ and 1366 $cm^{-1}$. The intensity of the former increases while the latter becomes a bit weak, suggesting that under light irradiation, the adsorption of $NH_3$ on the Lewis acid site is enhanced while the adsorption on the Bronsted acid site is mildly inhibited. Moreover, *in situ* IR spectra of $NH_3$-adsorbed $CaTiO_3$ were also collected and displayed in Fig. S10. The analysis of the spectra could be acquired in the supplementary information.

The characteristic absorption peaks of $NH_2$ species are generally distributed in the range of 1505-1580 $cm^{-1}$. [50] Nevertheless, none of such peaks appear in the dark or illuminated spectra, substantiating that the N-H bond from the chemisorbed $NH_3$ on 5Ce5Fe10Mn is hard to break at 125°C, even assisted by light irradiation.

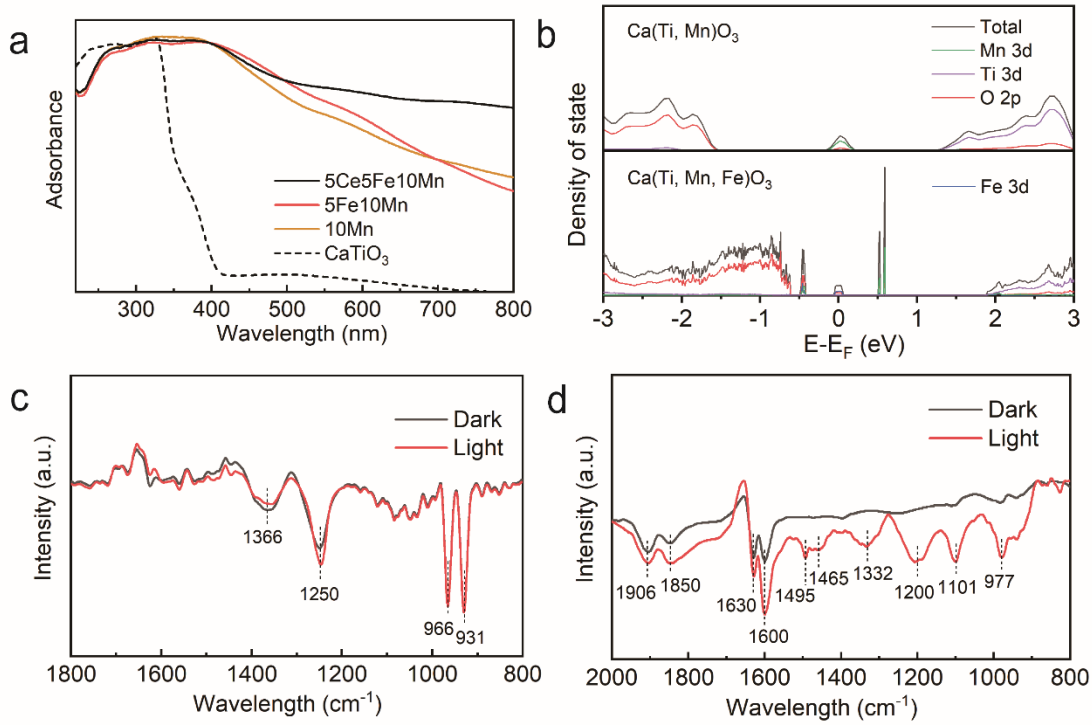


**Fig. 8. a**, UV-vis absorption spectra of the perovskite. **b**, PDOS of Ca(Ti, Mn)$O_3$ and Ca(Ti, Mn, Fe)$O_3$. **c**, *in situ* IR spectra of 5Ce5Fe10Mn with $NH_3$ adsorbed in the dark and visible light at 125°C; **d**, *in situ* IR spectra of 5Ce5Fe10Mn with NO + $O_2$ adsorbed in the dark and visible at 125°C.

There are four strong peaks in the dark spectra of 5Ce5Fe10Mn with NO + $O_2$ adsorbed (black line in Fig. 8d). These located at 1600 $cm^{-1}$ and 1630 $cm^{-1}$ are assigned to the bridged nitrate,[19] and those at 1850 $cm^{-1}$ and 1960 $cm^{-1}$ are ascribed to the weakly adsorbed NO species. The illuminated spectra (red line in Fig. 8d) show apparent differences from the dark counterpart. On the one hand, the intensities of the above four peaks become stronger. On the other, a series of strong peaks appear in the range from 1495 $cm^{-1}$ to 977 $cm^{-1}$. The peak at 1100 $cm^{-1}$ is assigned to nitrite monodentate species, [51] those around 1200 $cm^{-1}$, 1332 $cm^{-1}$, and 1465 $cm^{-1}$ are attributed to nitrites,[39, 42] and that at 1495 $cm^{-1}$

corresponds to monodentate nitrate. [48] These results manifest that light irradiation dramatically promotes NO oxidation rather than $NH_3$-to-$NH_2$ transformation. The variations of species on the 5Ce5Fe10Mn surface before and after light irradiation could also be observed in the infrared emission spectra in Fig. S11.

The NO-to-$NO_2$ conversion without $NH_3$ input was measured further to probe the optical effect on the SCR de$NO_x$. As depicted in Fig. S12, the NO-to-$NO_2$ conversion was about 22.5% at 125°C in the dark. With the light irradiation, the NO oxidation was boosted, and the NO-to-$NO_2$ conversion was significantly increased to about 33.2%. This result was coincident with that from the IR spectra in Fig. 8d, signifying that the optical excitation could promote the fast SCR process.

**4. Discussion**

It is widely accepted that $NH_2NO$ is a requisite in the cycle of standard SCR, but the involvement of $NH_4NO_2$ is in dispute. Powerful evidence by the time-resolved spectroscopy from Marberger et al. [10] showed that $NH_3$ coordinated to Bronsted site ($B_{NH_3}$) of $V_2O_5$-$WO_3$-$TiO_2$ does not participate in the catalytic cycle. $NH_3$ binding to Lewis sites ($L_{NH_3}$) could react with gaseous NO to form $NH_2NO$, generating a Bronsted acid site. However, if $L_{NH_3}$ could combine with this as-obtained Bronsted site, a new $B_{NH_3}$ is produced. This $B_{NH_3}$ could be consumed by forming $NH_4NO_2$ so that the total amount of $B_{NH_3}$ remains constant, also explaining the results of Figure 1 in ref 10. Therefore, the reaction mechanisms involving both $NH_2NO$ and $NH_4NO_2$ are also supported by Marberger's results. In our opinion, for the cycle of Standard SCR, $NH_4NO_2$ is another requisite intermediate to restore the clean surface of the perovskite.

No matter by Fe-Mn doping or light irradiation, the de$NO_x$ activity of modified $CaTiO_3$ mainly originates from the activation of NO. Hence, constructing photo-SCR catalysts from Ti-based perovskite should focus the principle issue on how to activate NO. Jonathan et al. [33] proposed that the binding strength of NO on perovskite surface depends on the B-site $e_g$ filling. Our results verified that NO adsorption rises as the $e_g$ filling increases from 0 of $CaTiO_3$ to 0.06 of Ca(Ti, Mn)$O_3$. The results also suggest that doping Ti-based perovskite with metal ions of $e_g$ filling greater than 0, such as $Co^{3+}$, and $Ni^{3+}$, could augment NO adsorption. Furthermore, doping $CaTiO_3$ simplifies the regulation of electronic structure on the optical property so that more attention could be put on how to activate NO. This strategy also extends the material range for photo-SCR de$NO_x$ to semiconductors of the wide bandgap.

A lot of enlightening studies [12, 13, 52, 53] reported that catalysts composed of different metal oxides are always superior to single metal oxide in terms of SCR performance. Most of the authors believed that the redox cycle between multivalent metal ions promotes NO-to-$NO_2$ oxidation, triggering the fast SCR reaction. Our results demonstrate that Fe-Mn doping of $CaTiO_3$ acts on the standard SCR by shortening the reaction pathway, providing new insights into the synergistic effect between multivalent metal ions.

Emphasizing the synergy between Fe and Mn does not mean that Ti is dispensible in this system. Instead, Ti of Ca(Ti, Mn, Fe)$O_3$ has two momentous effects in the SCR process. First, the $Ti_{5c}$ site selectively adsorbs $NH_3$, initiating the catalytic cycle by reacting with chemisorbed NO on the $Mn_{5c}$ site. The cooperation between Ti and Mn boosts the formation of $NH_2NO$, and is more efficient than that between two Mn sites since the high adsorption strength of NO on the $Mn_{5c}$ site, to some extent, inhibits

$NH_3$ adsorption along with $NH_2NO$ formation. Second, Ti 3d orbitals are the main components of the valence band, dictating the optical property of perovskite. Owing to the unique function of Ti, $CaTiO_3$ is a suitable framework for constructing efficient catalytic units for photo-SCR de$NO_x$.

$NH_3$-SCR de$NO_x$ involves three feeding gases, namely NO, $NH_3$, and $O_2$. A single type of active site may lead to excessive coverage of the catalyst surface by specific gas molecules, thus lowering the reaction efficiency. Compared with modulating gas adsorption strength, constructing disparate sites to selectively activate gas molecules could be a more feasible alternative to heighten the SCR reaction rate.

## 5. Conclusion

Ce-Fe-Mn doped $CaTiO_3$ for photo-SCR de$NO_x$ are abstracted from the titanium-bearing solid waste via a molten-salt method with sodium aluminosilicate as the flux. The dopants could well dissolve into $CaTiO_3$ and uniformly disperse in the perovskite solid solution. Both Fe and Mn atoms occupy the B sites of perovskite, while Ce is situated at the A site. The pristine $CaTiO_3$ has no catalytic activity for NO removal in 100-300°C, while (Ca, Ce)(Ti, Mn, Fe)$O_3$ could achieve nearly 100% NO conversion at 135°C under light irradiation (GHSV = 72000 $h^{-1}$). Mn dopant endows $CaTiO_3$ with impurity level to harvest visible light and exotic ability to capture gaseous NO molecules. With the incorporation of Fe into Ca(Ti, Mn)$O_3$, the NO-to-$NO_3^-$ oxidative center transfers from the five-coordinated Mn ($Mn_{5c}$) site to the $Fe_{5c}$ site, markedly shortening the reaction pathway of standard SCR. Further introduction of Ce into Ca(Ti, Mn, Fe)$O_3$ strengthens the response of perovskite to the light in the wavelength range from 500 nm to 800 nm. Moreover, illuminated *in situ* infrared (IR) spectra substantiate that the photocarriers intensify NO activation rather than the transformation from chemisorbed $NH_3$ to $NH_2$ radicals.

## Acknowledgments

This work was supported by the National Natural Science Foundation of China [grant numbers 51804005, U1660110].

## References

[1] K. Teramura, T. Tanaka, S. Yamazoe, K. Arakaki, T. Funabiki, Kinetic study of photo-SCR with $NH_3$ over $TiO_2$, Appl. Catal. B-Environ. 53(1) (2004) 29-36. https://doi.org/https://doi.org/10.1016/j.apcatb.2004.05.005.
[2] T. Tanaka, K. Teramura, T. Funabiki, Photoassisted selective catalytic reduction of NO with ammonia in the presence of oxygen at low temperature, Phys. Chem. Chem. Phys. 2(12) (2000) 2681-2682. https://doi.org/10.1039/B003264F.
[3] H. Zhang, X. Li, Y. Hui, L. Yu, Q. Xia, S. Luo, C. Yao, Development of $La_{1-x}Ce_xFeO_3$/attapulgite nanocomposites for photocatalytic reduction of NO at low temperature, J Mater Sci-Mater. El. 28(13) (2017) 9371-9377. https://doi.org/10.1007/s10854-017-6677-0.
[4] A. Yamamoto, K. Teramura, S. Hosokawa, T. Shishido, T. Tanaka, Visible-Light-Assisted Selective Catalytic Reduction of Nitric Oxide with Ammonia over Dye-Modified Titania Photocatalysts, ChemCatChem 7(12) (2015) 1818-1825. https://doi.org/https://doi.org/10.1002/cctc.201500207.
[5] X. Li, H. Shi, X. Yan, S. Zuo, Y. Zhang, Q. Chen, C. Yao, C. Ni, Rational construction of direct Z-scheme doped perovskite/palygorskite nanocatalyst for photo-SCR removal of NO: Insight into the effect of Ce incorporation, J. Catal. 369 (2019) 190-200. https://doi.org/https://doi.org/10.1016/j.jcat.2018.11.009.
[6] A. Yamamoto, Y. Mizuno, K. Teramura, S. Hosokawa, T. Shishido, T. Tanaka, Visible-light-assisted selective catalytic reduction of NO with $NH_3$ on porphyrin derivative-modified $TiO_2$ photocatalysts, Catal. Sci. Technol. 5(1) (2015) 556-561. https://doi.org/10.1039/C4CY00598H.
[7] G. He, Z. Lian, Y. Yu, Y. Yang, K. Liu, X. Shi, Z. Yan, W. Shan, H. He, Polymeric vanadyl species determine the low-temperature activity of V-based catalysts for the SCR of NOx with NH3, Sci. Adv. 4(11) (2018). https://doi.org/10.1126/sciadv.aau4637
[8] L. Han, S. Cai, M. Gao, J. Hasegawa, P. Wang, J. Zhang, L. Shi, D. Zhang, Selective Catalytic Reduction of $NO_x$ with $NH_3$ by Using Novel Catalysts: State of the Art and Future Prospects, Chem. Rev. 119(19) (2019) 10916-10976. https://doi.org/10.1021/acs.chemrev.9b00202

[9] L. Arnarson, H. Falsig, S.B. Rasmussen, J.V. Lauritsen, P.G. Moses, A complete reaction mechanism for standard and fast selective catalytic reduction of nitrogen oxides on low coverage $VO_x/TiO_2$(0 0 1) catalysts, J. Catal. 346 (2017) 188-197. https://doi.org/https://doi.org/10.1016/j.jcat.2016.12.017.
[10] A. Marberger, D. Ferri, M. Elsener, O. Kröcher, The Significance of Lewis Acid Sites for the Selective Catalytic Reduction of Nitric Oxide on Vanadium-Based Catalysts, Angew. Chem. Int. Edit. 55(39) (2016) 11989-11994. https://doi.org/https://doi.org/10.1002/anie.201605397.
[11] C. Paolucci, A.A. Verma, S.A. Bates, V.F. Kispersky, J.T. Miller, R. Gounder, W.N. Delgass, F.H. Ribeiro, W.F. Schneider, Isolation of the Copper Redox Steps in the Standard Selective Catalytic Reduction on Cu-SSZ-13, Angew. Chem. Int. Edit. 53(44) (2014) 11828-11833. https://doi.org/https://doi.org/10.1002/anie.201407030.
[12] T.H. Vuong, J. Radnik, J. Rabeah, U. Bentrup, M. Schneider, H. Atia, U. Armbruster, W. Grünert, A. Brückner, Efficient $VO_x/Ce_{1-x}Ti_xO_2$ Catalysts for Low-Temperature $NH_3$-SCR: Reaction Mechanism and Active Sites Assessed by in Situ/Operando Spectroscopy, ACS Catal. 7(3) (2017) 1693-1705. https://doi.org/10.1021/acscatal.6b03223.
[13] M. Zhu, J.-K. Lai, U. Tumuluri, Z. Wu, I.E. Wachs, Nature of Active Sites and Surface Intermediates during SCR of NO with $NH_3$ by Supported $V_2O_5$–$WO_3/TiO_2$ Catalysts, J. Am. Chem. Soc. 139(44) (2017) 15624-15627. https://doi.org/10.1021/jacs.7b09646.
[14] Q. Zhang, Y. Huang, S. Peng, Y. Zhang, Z. Shen, J.-j. Cao, W. Ho, S.C. Lee, D.Y.H. Pui, Perovskite $LaFeO_3$-$SrTiO_3$ composite for synergistically enhanced NO removal under visible light excitation, Appl. Catal. B-Environ. 204 (2017) 346-357. https://doi.org/10.1016/j.apcatb.2016.11.052.
[15] X. Li, Z. Wang, H. Shi, D. Dai, S. Zuo, C. Yao, C. Ni, Full spectrum driven SCR removal of NO over hierarchical $CeVO_4$/attapulgite nanocomposite with high resistance to $SO_2$ and $H_2O$, J. Hazard. Mater. 386 (2020). https://doi.org/10.1016/j.jhazmat.2019.121977.
[16] X. Li, H. Shi, W. Zhu, S. Zuo, X. Lu, S. Luo, Z. Li, C. Yao, Y. Chen, Nanocomposite $LaFe_{1-x}Ni_xO_3$ /Palygorskite catalyst for photo-assisted reduction of $NO_x$: Effect of Ni doping, Appl. Catai. B-Environ. 231 (2018) 92-100. https://doi.org/https://doi.org/10.1016/j.apcatb.2018.03.008.
[17] A. Yamamoto, Y. Mizuno, K. Teramura, T. Shishido, T. Tanaka, Effects of reaction temperature on the photocatalytic activity of photo-SCR of NO with $NH_3$ over a $TiO_2$ photocatalyst, Catal. Sci. Technol. 3(7) (2013) 1771-1775. https://doi.org/10.1039/C3CY00022B.
[18] K. Teramura, T. Tanaka, T. Funabiki, Photoassisted Selective Catalytic Reduction of NO with Ammonia in the Presence of Oxygen over $TiO_2$, Langmuir 19(4) (2003) 1209-1214. https://doi.org/10.1021/la0263918.
[19] G. Cheng, X. Liu, X. Song, X. Chen, W. Dai, R. Yuan, X. Fu, Visible-light-driven deep oxidation of NO over Fe doped $TiO_2$ catalyst: Synergic effect of Fe and oxygen vacancies, Appl. Catal. B-Environ. 277 (2020) 119196. https://doi.org/https://doi.org/10.1016/j.apcatb.2020.119196.
[20] W.T. Hong, M. Risch, K.A. Stoerzinger, A. Grimaud, J. Suntivich, Y. Shao-Horn, Toward the rational design of non-precious transition metal oxides for oxygen electrocatalysis, Energy Environ. Sci. 8(5) (2015) 1404-1427. https://doi.org/10.1039/C4EE03869J.
[21] H. Huang, R. Shi, X. Zhang, J. Zhao, C. Su, T. Zhang, Photothermal-assisted triphase photocatalysis over a multifunctional bilayer paper, Angew. Chem. Int. Edit. n/a(n/a) (2021). https://doi.org/https://doi.org/10.1002/anie.202110336.
[22] Y. Sun, L. Han, P. Strasser, A comparative perspective of electrochemical and photochemical approaches for catalytic $H_2O_2$ production, Chem. Soc. Rev. 49(18) (2020) 6605-6631. https://doi.org/10.1039/D0CS00458H.
[23] B. Weng, Z. Song, R. Zhu, Q. Yan, Q. Sun, C.G. Grice, Y. Yan, W.-J. Yin, Simple descriptor derived from symbolic regression accelerating the discovery of new perovskite catalysts, Nat. Commun. 11(1) (2020). https://doi.org/10.1038/s41467-020-17263-9.
[24] T.-H. Shen, L. Spillane, J. Vavra, P. Thi Ha My, J. Peng, Y. Shao-Horn, V. Tileli, Oxygen Evolution Reaction in $Ba_{0.5}Sr_{0.5}Co_{0.8}Fe_{0.2}O_{3\text{-delta}}$ Aided by Intrinsic Co/Fe Spinel-Like Surface, J. Am. Chem. Soc. 142(37) (2020) 15876-15883. https://doi.org/10.1021/jacs.0c06268.
[25] Z. Zhang, H. Lu, X. Li, X. Li, S. Ran, Z. Chen, Y. Yang, X. Wu, L. Li, Conversion of $CaTi_{1-x}Mn_xO_{3-\delta}$-Based Photocatalyst for Photocatalytic Reduction of NO via Structure-Reforming of Ti-Bearing Blast Furnace Slag, ACS Sustain. Chem. Eng. 7(12) (2019) 10299-10309. https://doi.org/https://doi.org/10.1021/acssuschemeng.9b00097.
[26] G. Kresse, J. Furthmuller, Efficiency of ab-initio total energy calculations for metals and semiconductors using a plane-wave basis set, Comp. Mater. Sci. 6(1) (1996) 15-50. https://doi.org/https://doi.org/10.1016/0927-0256(96)00008-0.
[27] G. Kresse, J. Hafner, Ab initio molecular-dynamics simulation of the liquid-metal–amorphous-semiconductor transition in germanium, Phys. Rev. B Condens. Matter. Mater. Phys. 49(20) (1994) 14251-14269. https://doi.org/https://doi.org/10.1103/PhysRevB.49.14251.
[28] J.P. Perdew, K. Burke, M. Ernzerhof, Generalized gradient approximation made simple, Phys. Rev. Lett. 77(18) (1996) 3865-3868. https://doi.org/https://doi.org/10.1103/PhysRevLett.77.3865.
[29] S. Sasaki, C.T. Prewitt, J.D. Bass, W.A. Schulze, Orthorhombic perovskite $CaTiO_3$ and $CdTiO_3$: structure and space group, Acta Crystallogr. C 43(9) (1987) 1668-1674. https://doi.org/doi:10.1107/S0108270187090620.
[30] J. Mu, X. Li, W. Sun, S. Fan, X. Wang, L. Wang, M. Qin, G. Gan, Z. Yin, D. Zhang, Inductive Effect Boosting Catalytic Performance of Advanced $Fe_{1-x}V_xO_\delta$ Catalysts in Low-Temperature $NH_3$ Selective Catalytic Reduction: Insight into the Structure, Interaction, and Mechanisms, ACS Catal. 8(8) (2018) 6760-6774. https://doi.org/10.1021/acscatal.8b01196.
[31] K. Wang, V. Fung, Z. Wu, D.-e. Jiang, Stable Surface Terminations of a Perovskite Oxyhydride from First Principles, J. Phys. Chem. C 124(34) (2020) 18557-18563. https://doi.org/10.1021/acs.jpcc.0c03956.
[32] H. Wang, G. Wang, X. Wei, J. Cui, First-principles study of $CaTiO_3$ oxygen-vacancies (001) surface, Physica

B 407(19) (2012) 3970-3974. https://doi.org/https://doi.org/10.1016/j.physb.2012.06.022.
[33] J. Hwang, R.R. Rao, L. Giordano, Y. Katayama, Y. Yu, Y. Shao-Horn, Perovskites in catalysis and electrocatalysis, Science 358(6364) (2017) 751-756. https://doi.org/10.1126/science.aam7092.
[34] Y. Peng, K. Li, J. Li, Identification of the active sites on $CeO_2$–$WO_3$ catalysts for SCR of $NO_x$ with $NH_3$: An in situ IR and Raman spectroscopy study, Appl. Catal. B-Environ. 140-141 (2013) 483-492. https://doi.org/https://doi.org/10.1016/j.apcatb.2013.04.043.
[35] Z. Chen, Q. Yang, H. Li, X. Li, L. Wang, S. Chi Tsang, Cr–$MnO_x$ mixed-oxide catalysts for selective catalytic reduction of $NO_x$ with $NH_3$ at low temperature, J. Catal. 276(1) (2010) 56-65. https://doi.org/https://doi.org/10.1016/j.jcat.2010.08.016.
[36] H. Chang, X. Chen, J. Li, L. Ma, C. Wang, C. Liu, J.W. Schwank, J. Hao, Improvement of Activity and $SO_2$ Tolerance of Sn-Modified $MnO_x$–$CeO_2$ Catalysts for $NH_3$-SCR at Low Temperatures, Environ. Sci. Technol. 47(10) (2013) 5294-5301. https://doi.org/10.1021/es304732h.
[37] M. Salazar, R. Becker, W. Grunert, Hybrid catalysts-an innovative route to improve catalyst performance in the selective catalytic reduction of NO by $NH_3$, Appl. Catal. B-Environ. 165 (2015) 316-327. https://doi.org/10.1016/j.apcatb.2014.10.018.
[38] T.V.W. Janssens, H. Falsig, L.F. Lundegaard, P.N.R. Vennestrøm, S.B. Rasmussen, P.G. Moses, F. Giordanino, E. Borfecchia, K.A. Lomachenko, C. Lamberti, S. Bordiga, A. Godiksen, S. Mossin, P. Beato, A Consistent Reaction Scheme for the Selective Catalytic Reduction of Nitrogen Oxides with Ammonia, ACS Catal. 5(5) (2015) 2832-2845. https://doi.org/10.1021/cs501673g.
[39] H. Liu, Z.X. Fan, C.Z. Sun, S.H. Yu, S. Feng, W. Chen, D.Z. Chen, C.J. Tang, F. Gao, L. Dong, Improved activity and significant $SO_2$ tolerance of samarium modified $CeO_2$-$TiO_2$ catalyst for NO selective catalytic reduction with $NH_3$, Appl. Catal. B-Environ. 244 (2019) 671-683. https://doi.org/10.1016/j.apcatb.2018.12.001.
[40] N.-I. Kim, S.-H. Cho, S.H. Park, Y.J. Lee, R.A. Afzal, J. Yoo, Y.-S. Seo, Y.J. Lee, J.-Y. Park, B-site doping effects of $NdBa_{0.75}Ca_{0.25}Co_2O_{5+\delta}$ double perovskite catalysts for oxygen evolution and reduction reactions, J. Mater. Chem. A 6(36) (2018) 17807-17818. https://doi.org/10.1039/C8TA06236F.
[41] Q. Wu, R. Van de Krol, Selective Photoreduction of Nitric Oxide to Nitrogen by Nanostructured $TiO_2$ Photocatalysts: Role of Oxygen Vacancies and Iron Dopant, J. Am. Chem. Soc. 134 (2012) 9369-75. https://doi.org/10.1021/ja302246b.
[42] X. Huang, F. Dong, G. Zhang, Y. Guo, Z. Tang, A strategy for constructing highly efficient yolk-shell Ce@Mn@$TiO_x$ catalyst with dual active sites for low-temperature selective catalytic reduction of NO with $NH_3$, Chem. Eng. J. 419 (2021) 129572. https://doi.org/https://doi.org/10.1016/j.cej.2021.129572.
[43] W. Si, H. Liu, T. Yan, H. Wang, J. Li, Sn-doped rutile $TiO_2$ for vanadyl catalysts: Improvements on activity and stability in SCR reaction, 269 (2020) 118797-.
[44] J. Liu, X. Li, R. Li, Q. Zhao, J. Ke, H. Xiao, L. Wang, S. Liu, M. Tadé, S. Wang, Facile synthesis of tube-shaped Mn-Ni-Ti solid solution and preferable Langmuir-Hinshelwood mechanism for selective catalytic reduction of $NO_x$ by $NH_3$, 549 (2018) 289-301. https://doi.org/https://doi.org/10.1016/j.apcata.2017.10.010.
[45] S. Roy, B. Viswanath, M.S. Hegde, G. Madras, Low-Temperature Selective Catalytic Reduction of NO with $NH_3$ over $Ti_{0.9}M_{0.1}O_{2-\delta}$ (M = Cr, Mn, Fe, Co, Cu), 112(15) (2008) 6002-6012.
[46] Shijian, Yang, and, Chizhong, Wang, and, Junhua, Li, and, Naiqiang, Low temperature selective catalytic reduction of NO with $NH_3$ over Mn–Fe spinel: Performance, mechanism and kinetic study, (2011).
[47] Y. Inomata, H. Kubota, S. Hata, E. Kiyonaga, K. Morita, K. Yoshida, N. Sakaguchi, T. Toyao, W. Ueda, M. Haruta, T. Murayama, Bulk tungsten-substituted vanadium oxide for low-temperature $NO_x$ removal in the presence of water, Nat. Commun. 12 (2021). https://doi.org/10.1038/s41467-020-20867-w.
[48] Y. Liu, T. Gu, X. Weng, Y. Wang, Z. Wu, H. Wang, DRIFT Studies on the Selectivity Promotion Mechanism of Ca-Modified Ce-Mn/$TiO_2$ Catalysts for Low-Temperature NO Reduction with NH3, J. Phys. Chem. C 116(31) (2012) 16582-16592. https://doi.org/10.1021/jp304390e.
[49] F. Liu, W. Shan, Z. Lian, J. Liu, H. He, The smart surface modification of $Fe_2O_3$ by $WO_x$ for significantly promoting the selective catalytic reduction of $NO_x$ with $NH_3$, Appl. Catal. B-Environ. 230 (2018) 165-176. https://doi.org/https://doi.org/10.1016/j.apcatb.2018.02.052.
[50] G. Busca, L. Lietti, G. Ramis, F. Berti, Chemical and mechanistic aspects of the selective catalytic reduction of NOx by ammonia over oxide catalysts: A review, Appl. Catal. B-Environ. 18(1) (1998) 1-36. https://doi.org/https://doi.org/10.1016/S0926-3373(98)00040-X.
[51] M. Adamowska, A. Krztoń, M. Najbar, P. Da Costa, G. Djéga-Mariadassou, DRIFT study of the interaction of NO and $O_2$ with the surface of $Ce_{0.62}Zr_{0.38}O_2$ as de$NO_x$ catalyst, Catal. Today 137(2) (2008) 288-291. https://doi.org/https://doi.org/10.1016/j.cattod.2008.01.013.
[52] Z. Liu, G. Sun, C. Chen, K. Sun, L. Zeng, L. Yang, Y. Chen, W. Wang, B. Liu, Y. Lu, Y. Pan, Y. Liu, C. Liu, Fe-Doped $Mn_3O_4$ Spinel Nanoparticles with Highly Exposed Feoct–O–Mntet Sites for Efficient Selective Catalytic Reduction (SCR) of NO with Ammonia at Low Temperatures, ACS Catal. 10(12) (2020) 6803-6809. https://doi.org/10.1021/acscatal.0c01284.
[53] C. Liu, F. Li, J. Wu, X. Hou, W. Huang, Y. Zhang, X.G. Yang, A comparative study of $MO_x$ (M = Mn, Co and Cu) modifications over $CePO_4$ catalysts for selective catalytic reduction of NO with $NH_3$, J. Hazard. Mater. 363 (2019) 439-446. https://doi.org/10.1016/j.jhazmat.2018.09.054.